Article

Controlling the Structure and Morphology of Organic Nanofilaments Using External Stimuli

Barış Sezgin, Jiao Liu, Diana P. N. Gonçalves, Chenhui Zhu, Tahir Tilki, Marianne E. Prévôt,* and Torsten Hegmann*

Cite This: https://doi.org/10.1021/acsnanoscienceau.3c00005

Read Online

ACCESS | Metrics & More | Article Recommendations | Supporting Information

ABSTRACT: In our continuing pursuit to generate, understand, and control the morphology of organic nanofilaments formed by molecules with a bent molecular shape, we here report on two bent-core molecules specifically designed to permit a phase or morphology change upon exposure to an applied electric field or irradiation with UV light. To trigger a response to an applied electric field, conformationally rigid chiral (S,S)-2,3-difluorooctyloxy side chains were introduced, and to cause a response to UV light, an azobenzene core was incorporated into one of the arms of the rigid bent core. The phase behavior as well as structure and morphology of the formed phases and nanofilaments were analyzed using differential scanning calorimetry, cross-polarized optical microscopy, circular dichroism spectropolarimetry, scanning and transmission electron microscopy, UV−vis spectrophotometry, as well as X-ray diffraction experiments. Both bent-core molecules were characterized by the coexistence of two nanoscale morphologies, specifically helical nanofilaments (HNFs) and layered nanocylinders, prior to exposure to an external stimulus and independent of the cooling rate from the isotropic liquid. The application of an electric field triggers the disappearance of crystalline nanofilaments and instead leads to the formation of a tilted smectic liquid crystal phase for the material featuring chiral difluorinated side chains, whereas irradiation with UV light results in the disappearance of the nanocylinders and the sole formation of HNFs for the azobenzene-containing material. Combined results of this experimental study reveal that in addition to controlling the rate of cooling, applied electric fields and UV irradiation can be used to expand the toolkit for structural and morphological control of suitably designed bent-core molecule-based structures at the nanoscale.

KEYWORDS: bent-core liquid crystal, B4 phase, morphology, chirality, electric field, UV irradiation
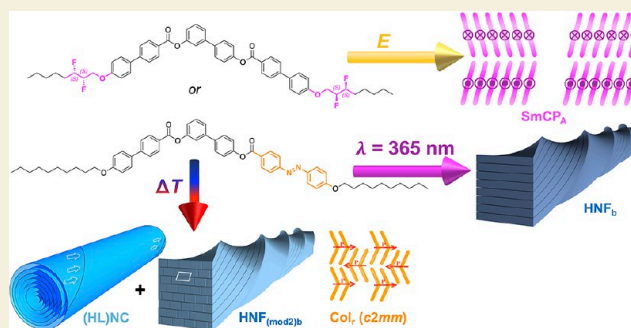
1. INTRODUCTION

Structure and morphology (or shape) control in nano- and microstructures is an active field of research largely driven by mimicking nature's ability to proactively respond to external stimuli.[1] To illustrate just a few, chameleons achieve active and rapid color change by tuning the lattice of guanine nanocrystals,[2] cephalopods use reversible soft tissue shape changes for camouflage,[3] and *Boquila trifoliolata*—a vine plant from rainforests in southern Chile—is capable of complex leaf mimicry (shape, color, and orientation), potentially using communication through volatile chemicals or acoustic signals to actively imitate the leaf character of surrounding plants of other species.[4] External stimuli to realize structural or morphological changes commonly include changes in pH,[5] changes in temperature,[6] mechanical deformation,[7] exposure to chemicals,[8] irradiation with light at specific wavelengths,[9−13] and external electric or magnetic fields.[14−16] Considering our ongoing discoveries of nanofilament shapes (morphologies) in the B4 phase of some bent-core liquid crystals (BC-LCs),[17] we were particularly intrigued by the opportunity to alter the

nanofilament shape using external stimuli other than the rate of temperature change on cooling from an isotropic liquid. Here, applying an electric field or irradiation with UV light was of particular interest.

Morphological variations of the so-called B4 phase (morphology, from the Greek root morpho- meaning shape and defined as the study of shape) now include helical nanofilaments (HNFs[18]) with varying dimensions (width and pitch) as well as intra- or interlayer modulation (HNF_{mod2a} and HNF_{mod2b}) as well as helical microfilaments,[18−23] heliconical nanocrystallites,[24] helicoidal-layered nanocylinders (HLNCs),[25] and flat or twisted nanoribbons.[26] Practically, all these filament-, ribbon-, and layered nanocylinder-based B4
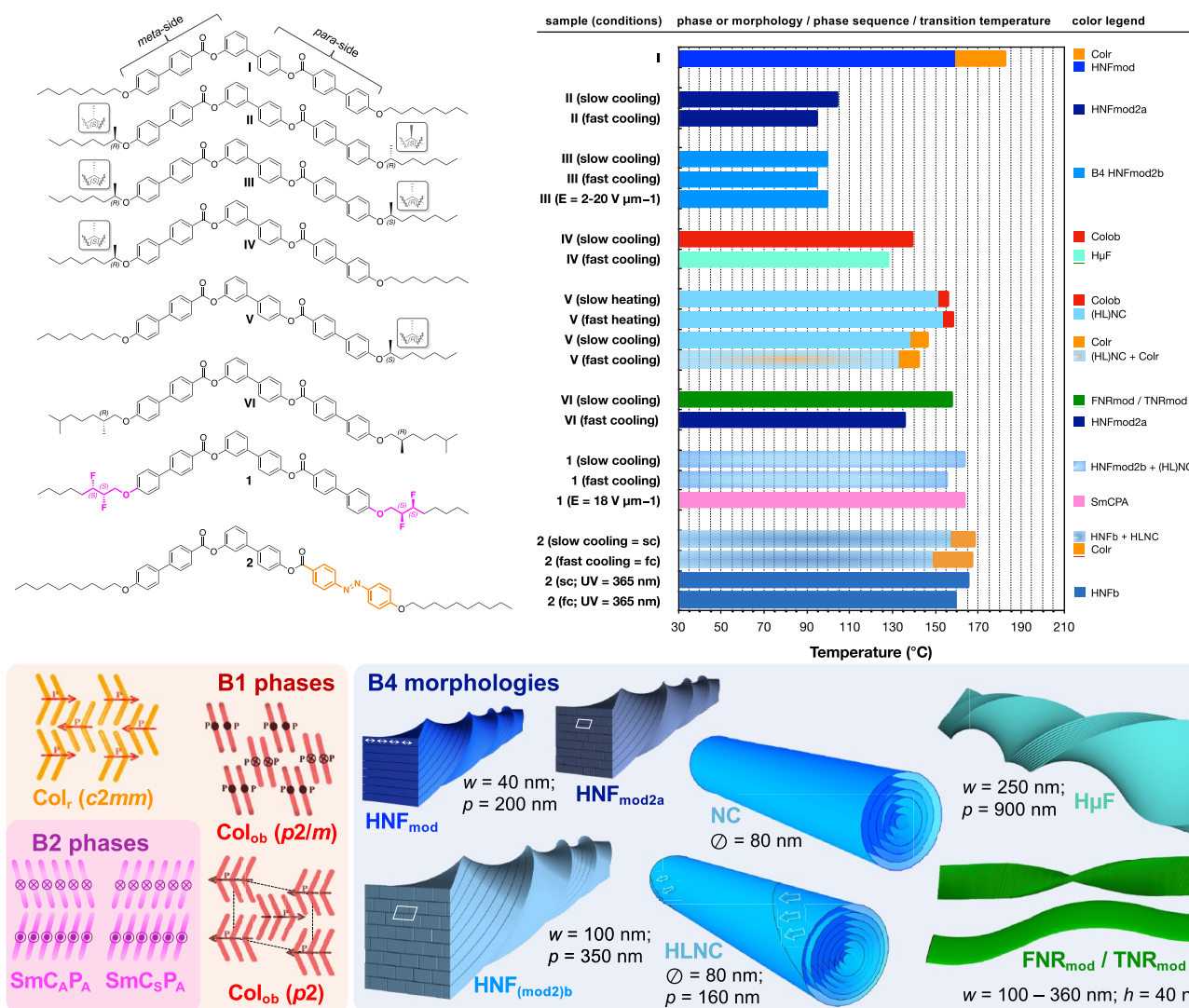
A

Figure 1. Comparison of the phase sequence, phase structure, B4 morphology, and phase transition temperatures depending on the chemical structure—position, branching points, as well as the number and configuration of chiral center(s) in the aliphatic side chains—of the parent compounds I−VI[20,22,23,25,26] (chiral center configurations only affect the handedness of the final filaments) with the here-investigated new compounds **1** and **2** (Arabic numerals). Models for the different B1 and B2 phase structures as well as the B4 morphologies are shown at the bottom. The color coding in the bar diagram and models is used throughout in the data plots for various B4 morphologies and B1 or B2 phases.

morphologies were realized by strategically incorporating chiral centers into the aliphatic side chains of bent-core molecules featuring up to three biphenyl structural segments.[19] Notably, all B4 nano- and microscale morphologies display a characteristic blue structural color (in reflection mode),[27,28] whose origin is not entirely understood but certainly linked to diffraction, scattering, or interference via the periodic nano- to microscale layering and packing of these filaments in the ensuing bulk thin films.[29] Furthermore, several of these materials displayed intriguing polymorphisms[22,25,26] that were, until now, driven exclusively by differences in the cooling rate from the isotropic liquid phase (summarized in Figure 1 for the parent compounds using Roman numerals I−VI): increasing or decreasing (compounds I and V), heating or cooling (compound V), or alternatively by varying the cooling rate after heating the materials to the isotropic liquid state (compounds IV and VI).

Compound IV showed polymorphism depending on the cooling rate from the isotropic liquid phase with the formation

of a B1 rectangular columnar phase ($Col_{ob}-p2/m$) on slow cooling (≤5 °C min^{-1}) and B4 helical microfilaments (HμF) on rapid cooling (~50 °C min^{-1}),[22] while compound V showed such polymorphism only for the columnar phases, forming HLNCs on both heating and cooling, sometimes in phase coexistence with the high-temperature B1 phase: $Col_{ob}-p2$ on heating and Col_r-c2mm on cooling.[25] Instead, compound VI showed B4 polymorphism exclusively with the formation of different B4 filaments depending on the rate of cooling from the isotropic liquid phase.[26] All this was achieved by strategically placing chiral centers into aliphatic side chains and altering their number, position, and configuration. Molecular conformational analyses revealed that these structural changes in chiral side chains primarily affected the overall molecular conformation (particularly focusing on the dihedral angle at the core-chain juncture)[25] and, as a result thereof, the morphology of the B4 building blocks.

By making two further strategic molecular changes to these tris-biphenyl BC-LCs, the aim of the current work was to
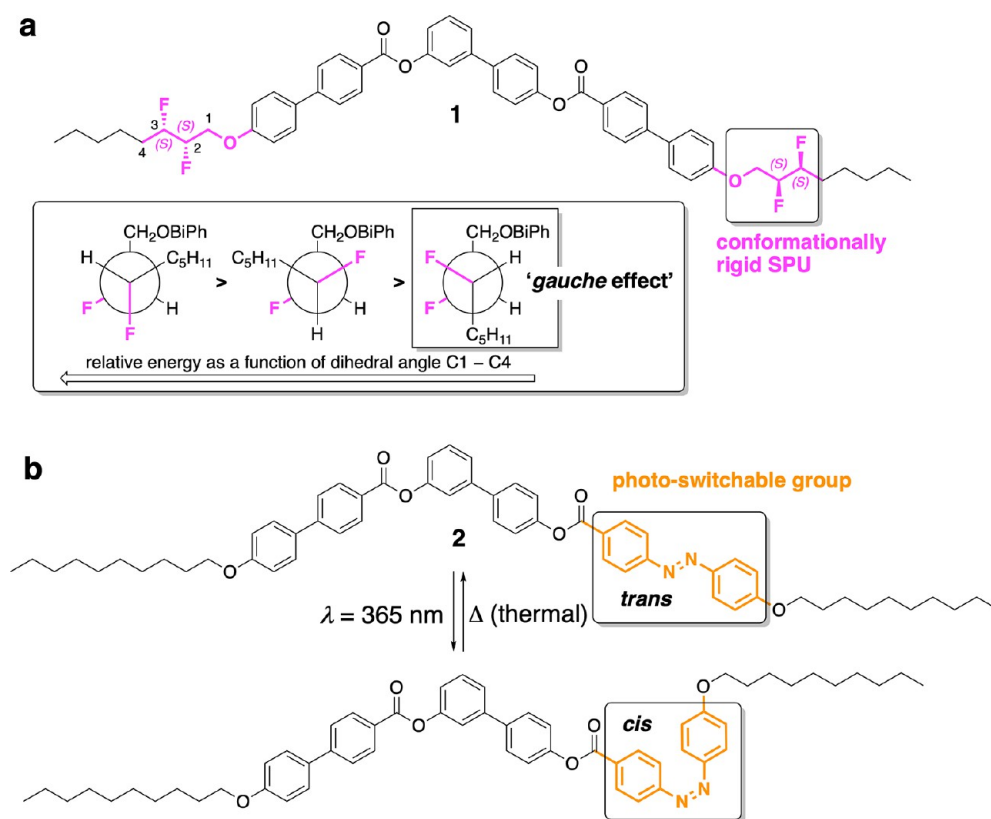
Figure 2. BC-LC compounds with structural motives facilitating phase or morphological changes in response to external stimuli: (a) **1** with two (*S*,*S*)-2,3-difluorooctyloxy chiral side chains potentially responsive to an applied electric field, and (b) **2** with an azobenzene unit in the longer para-arm that may be triggerable toward shape or phase changes by irradiation with the UV light at a short wavelength (e.g., λ = 365 nm) as a result of an ensuing trans-to-cis photoisomerization and thermal back relaxation.

regulate the phase or morphology by either applying an electric field or by irradiating the sample with UV light. Across the materials and length scale spectrum, these two external stimuli have been extensively employed to afford structural and morphological changes. Applied electric fields have been used to alter ("square") the shape of giant vesicles,[14] control morphological evolution in thin silicon rubber films,[15] or alter the phase (from CuO to Cu$_2$O) and shape (spherical to elongated leaf-like) of copper oxide nanostructures,[16] among others. Light-controlled shape changes are even more prevalent in the literature, largely because of the attractive, non-invasive remote actuation permitted by light irradiation.[11] Light-induced swelling was shown for stratified (layer-by-layer assembled) polymer-grafted gold nanoparticles and homopolymers,[13] and all sorts of pre-programmed shape changes have been demonstrated for a large number of polymers and elastomers (many of them liquid crystalline[30−41]), as well as a wide range of other materials and material combinations[42−47] with a common trait being the functionalization with organic photoswitches.[48−65] Among them, azobenzene is conceivably the most rigorously used and studied,[66] which is why we employed this structural motive here as well.

An applied electric field has previously been used to generate chiral memory during the thermal transitions (temperature cycling) between the B2 and B4 phases of an achiral BC-LC system with an Iso−B2−B4 phase sequence on cooling. Homochiral SmC$_A$P$_A$ (anticlinic antiferroelectric) and racemic SmC$_S$P$_A$ (synclinic antiferroelectric) smectic-C textures were prepared by subjecting a thin film of the BC-LC material, sandwiched between two indium tin oxide (ITO)-coated glass slides, to specific waveforms and varying magnitudes (up to 10 V μm^{-1}) of an applied electric field. Temperature cycling between the B4 and B2 phases then led to the generation of the homochiral SmC$_A$P$_A$ texture but not to any change in the phase structure or morphology.[67] Previous work by our group showed that applying an electric field up to the same magnitude of 10 V μm^{-1} (triangular or square waveform) to the HNF$_{mod2a}$ or HNF$_{mod2b}$ formed by compounds **II** or **III** did not lead to any changes in texture or phase.[20,23] Thin-film preparation between ITO-coated glass slides (cell gap: 5 μm) persisted in showing the typical bluish focal conic-like textures as well as the blue structural color in reflection, thereby indicating that the applied electric field had no effect on the already formed B4 phase with HNF$_{mod2}$ morphology. To increase our chances that an applied electric field will trigger a phase or morphological change, we introduced (*S*,*S*)-2,3-difluorooctyloxy aliphatic side chains, which add two conformationally rigid stereopolar units (SPU)[68,69] to the molecular framework (Figure 2a). Previous studies have shown that chiral 2,3-difluoroalkyloxy side chains exhibit relatively large polarization powers when added as chiral solutes to induce ferroelectric LC mixtures.[68] Calculated conformational energy profiles revealed that greater conformational rigidity about the C-2−C-3 bond axis is due to the repulsive interaction of the two fluoro-substituents and the "gauche effect" associated with this structural unit (i.e., the hyperconjugative interactions between vicinal C−H and C−F bonds as in the lowest energy conformation highlighted on the right in Figure 2a). Furthermore, a twisted orientation of the two arms that usually gives rise to HNF formation would bring the

two SPUs closer to the same side of the BC-LC molecule[25] and permit a response to an electric field from both conformationally rigid core-chain juncture segments.

With respect to UV light as a trigger for a phase or morphological change, we decided to focus first on the member of this family that incorporates the azobenzene unit into one of the arms of the BC-LC molecule. BC-LCs with azobenzene motives forming HNFs have been reported previously, and in the reported experiments, the azobenzene units permitted an alignment of the HNFs based on the Weigert effect[70,71] (where after successive, reversible photo-isomerization, the equilibrium state is biased toward the trans-isomer that is thermodynamically more stable than the cis-isomer, which ultimately leads to a molecular orientation in a direction parallel to the impinging UV light irradiation).[27,28] Other instances introduced azobenzenes into BC-LCs by replacing phenyl benzoate arms attached via ester linkages to a 3,4′-dihydroxybiphenyl central core. When introduced into the longer para-arm, the formation of a SmC$_A$P$_A$ phase was reported, while replacing both phenyl benzoates with azobenzene led to a Col$_{ob}$ phase, but no B4 phase,[72] perhaps already highlighting the significance of retaining at least one of the biphenyl arms (Figure 2b). Furthermore, placing the azobenzene unit into the longer para-arm could result in a sufficient conformational difference in the core-chain juncture[25] so as to permit the formation of the layered nanocylinder (NC, HLNC) morphology that could then be suppressed by UV light irradiation in favor of aligned HNFs by the earlier mentioned Weigert effect.

With these considerations in mind, we synthesized compounds **1** and **2** and fully studied their phase behavior under varying cooling rates from the isotropic liquid phase as well as upon exposure to the above-indicated external stimuli, an applied electric field for **1** and UV irradiation for **2**, by polarized optical microscopy (POM), differential scanning calorimetry (DSC), both scanning and transmission electron microscopy (SEM and TEM), thin-film circular dichroism (CD) spectropolarimetry (only for the chiral compound **1**), and X-ray diffraction (XRD) using a laboratory or a synchrotron source.

2. MATERIALS AND METHODS

2.1. Synthesis

The synthesis of compounds **1** and **2** followed methods reported by our group previously.[20−23,25,26] The synthesis of (S,S)-2,3-difluor-ooctyl tosylate for compound **1** and the subsequent substitution reaction were done following procedures described by Lemieux and co-workers.[68,69] The synthetic pathways, synthesis details, and all analytical data for the two BC-LC compounds are detailed in the Supporting Information (Section S1, Schemes S1 and S2, as well as Figures S1−S9).

2.2. Optical and Thermal Characterization

POM studies were carried out using an Olympus BX-53 polarizing microscope equipped with a Linkam LTS420E heating/cooling stage. Samples were heated above the clearing point, as indicated by DSC, and then cooled at either <5 °C min^{-1} (commonly at 2 °C min^{-1}; slow cooling) or ≥50 °C min^{-1}. The phase transition temperatures and enthalpies were measured using either a PerkinElmer Pyris 1 DSC or a Perkin Elmer DSC-7 at two heating/cooling rates (either at 5 °C min^{-1} or at 50 °C min^{-1}), reporting data from the second heating/cooling runs, respectively. The temperature was calibrated with indium and zinc standards.

2.3. Spectroscopy and Spectropolarimetry

UV−vis and thin-film CD data were acquired using an OLIS spectrophotometer suite using quartz cuvettes and flat quartz substrates. Illumination with UV light at a wavelength of λ = 365 nm for UV−vis was accomplished using a UVCureMXLED LED light curing spot gun (P = 6 W). For thin film CD measurements, to eliminate contributions from linear dichroism and birefringence, all samples and sample areas were investigated at 45° interval sample rotation angles. The spectra were then summed up to provide genuine CD signals of the sample area.[73] The area interrogated by the light beam, given by the instrumental slit size and shape, is ∼0.4 cm in diameter and larger than most individual domains seen by the POM of the samples sandwiched between two quartz substrates using nominal spacers of 10 μm.

2.4. X-ray Diffraction

Variable-angle XRD was carried out on beamline 7.3.3 of the Advanced Light Source (ALS) of the Lawrence Berkeley National Laboratory[74] (10 keV incident beam energy, 1.24 Å wavelength, utilizing a Pilatus 2 M detector; beam: 500 mA, 10 s exposure, spot size of 250 × 800 μm, in air). Materials were filled into 1 mm diameter quartz X-ray capillary tubes, which were then mounted into a custom-built aluminum cassette that allowed X-ray detection with a ±13.5° angular range. A silver behenate standard was used to calibrate the detector distance and beam center, and the calibrated 2D images were converted to radially integrated 1D curves using the NIKA SAXS data reduction software.[75] Temperature-controlled XRD experiments were also performed with an in-house Xenocs Xeuss 3.0 using a Cu Kα source (λ = 1.54 Å) equipped with a Linkam HFSX350 heating/cooling stage. This setup also allows for in vacuo POM (see Supporting Information for further details and images), where the sample can be imaged and domains of interest marked, which are subsequently interrogated by the X-ray beam. The sample compartment also permitted UV irradiation during data acquisition using the UV LED spot gun. The difference in spot size with respect to the relative dimensions at ALS and the in-house X-ray instrument of the domains in samples showing phase coexistence allowed for a comparison of more local vs more global data sets.

2.5. SEM and TEM

SEM analysis was performed using a Quanta 450 FEG SEM commonly without prior metal deposition. TEM was carried out on an FEI Tecnai F20 microscope, operating at 200 kV, and equipped with a Schottky field emission gun and a twin-blade anticontaminator. All images were recorded using a Gatan 4K Ultra Scan charge-coupled device camera. Since these organic material films are sensitive to the electron beam irradiation, the films were normally previewed rapidly at a dose of 20 e$^-$ nm^{-2}. Selected areas were then imaged at a dose level of 200 e$^-$ nm^{-2}, which did not cause radiation damage. A drop of a solution of each compound in an organic solvent such as CH$_2$Cl$_2$ or n-hexane was placed on either ITO substrates for SEM or carbon-coated Cu grids for TEM. After complete evaporation of the solvent in vacuum, the sample was heated and cooled as described for the POM experiments.

2.6. Specifics of Sample Preparation

To apply electric fields, 6 μm films were prepared by filling **1** by capillary forces into ITO-coated cells with rubbed polyimide alignment layers favoring planar anchoring using an electrooptic setup consisting of an HP 33120A function generator amplified by a FLC E20AD voltage amplifier. UV illumination of compound **2** for POM, SEM, TEM, and XRD experiments used the same UV source as indicated for UV−vis spectroscopy data acquisition.

3. RESULTS AND DISCUSSION

Figure 1 already provides an overview of the phase sequence (type and transition temperatures) and B4 morphology observed for compounds **1** and **2** under different experimental conditions. In what follows, we will detail our experimental
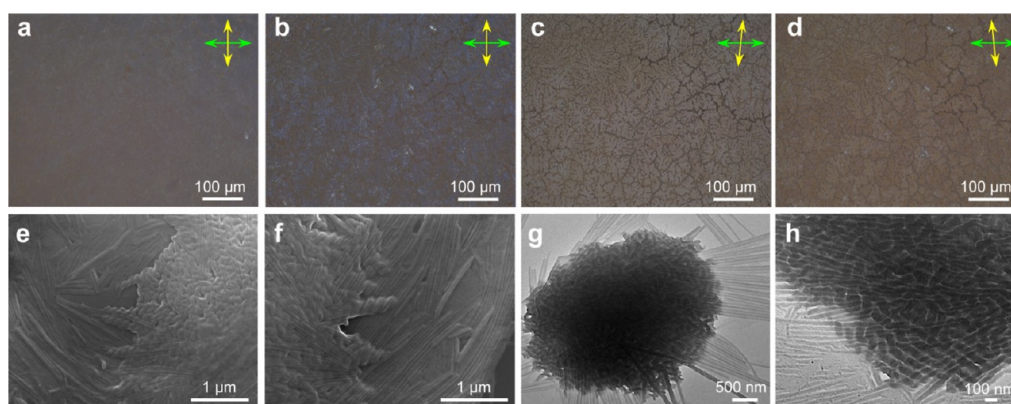
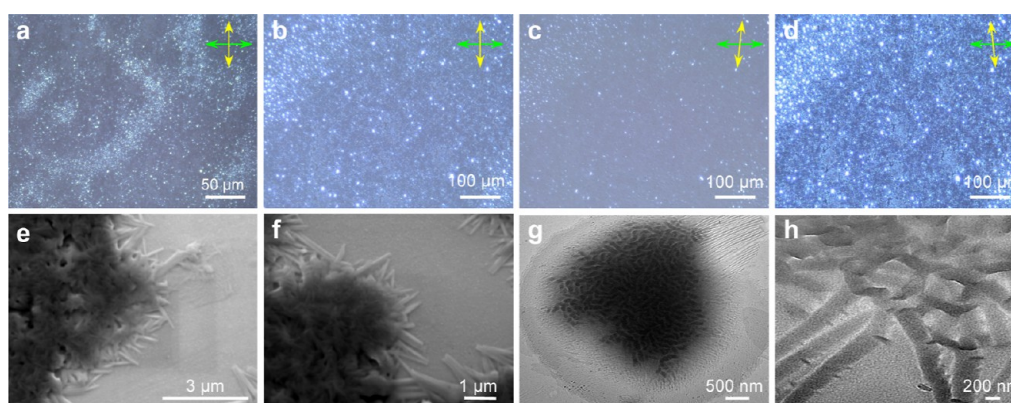**Figure 3.** Polarized optical photomicrographs (compound **1**) after heating to the isotropic liquid phase (>175 °C) and subsequent slow cooling to room temperature (~20 °C) at the cooling rate of 5 °C min^{-1}: (a) crossed polarizers at T = 160 °C, (b) crossed polarizers at T = 20 °C, and (c,d) ± 6° decrossed polarizers at T = 20 °C. (e,f) SEM images after heating to the isotropic liquid phase followed by slow cooling to room temperature (different domains). (g,h) TEM images obtained upon slow cooling.

Figure 4. Polarized optical photomicrographs (compound **1**) after heating to the isotropic liquid phase (>175 °C) and subsequent rapid cooling to room temperature (~20 °C) at the cooling rate ≥50 °C min^{-1}: (a,b) crossed polarizers at T = 20 °C, (c,d) ± 6° decrossed polarizers at T = 20 °C. (e,f) SEM images (different domains) after heating to the isotropic liquid phase followed by rapid cooling to room temperature. (g,h) TEM images obtained after rapid cooling (thermal quench).

findings and compare them to those of closely related analogues among compounds **I−VI** shown in the bar diagram.

3.1. Compound 1 with (S,S)-2,3-Difluorooctyloxy Side Chains

On heating as well as on cooling from the resulting isotropic liquid phase at a rate of 5 °C min^{-1} (slow cooling = sc), respectively, **1** only shows one phase transition by POM and DSC (Figure S10a, and Table S1). The appearance of **1** observed by POM is initially (i.e., at elevated temperatures) characterized by a low birefringence fern leaf-like and bluish texture, and the birefringence then gradually increases as one approaches room temperature (Figure 3a,b). The textural features overall are quite reminiscent of those previously observed and described for two of the parent compounds **I** and **V** under similar experimental conditions. Decrossing polarizer and analyzer in the opposite direction only changes the overall brightness of the texture, but no toggling between adjacent bright and dark domains was discernible (Figure 3c,d), which is expected given the homochiral nature of compound **1**.[18] Homochiral compounds such as **II** and **III** showed the exact same textural feature.

With the typical bluish texture observed by POM potentially signaling the existence of a B4 morphology, SEM and TEM imaging confirmed this hypothesis. Interestingly, both SEM

and TEM images show a coexistence of two B4 morphologies, one previously seen for compounds **I−III**[20,23] and another one seen for compound **V**[25], here combined in the form of mixed crystals composed of the two polymorphs since the two morphologies can hardly be considered independent structures in some area of the samples imaged. The HNFs are on average about 100 nm in width with a helical pitch of about 300−400 nm and are exclusively left-handed (Figure 3e,f and Supporting Information, Figure S11). Considering the positions and configurations of the chiral centers, compound **VI** is here the closest analogue, and **VI** formed the HNF$_{mod2a}$ morphology only upon rapid and not on slow cooling and formed both left- as well as right-handed filaments due to the diminished chirality as the chiral center was moved away from the core-chain juncture.[26] However, given the conformational rigidity of the chiral 2,3-difluorooxy segment at this core-chain juncture, the homochiral HNFs observed here are not surprising. Given all we know about altering the configuration and the position of chiral centers along aliphatic side chains, compound **1** with an (S,S)-configuration at C2 should form left-handed HNFs just like compound **II** with an (S,S) configuration at C1, following earlier applied Gray & McDonnell rules for predicting the handedness of chiral nematic (N*) phases[76] (chiral substituents at C1 for **II** and at C2 for **1** are on the same sides of the molecule, Figure S12). Puzzling are the larger
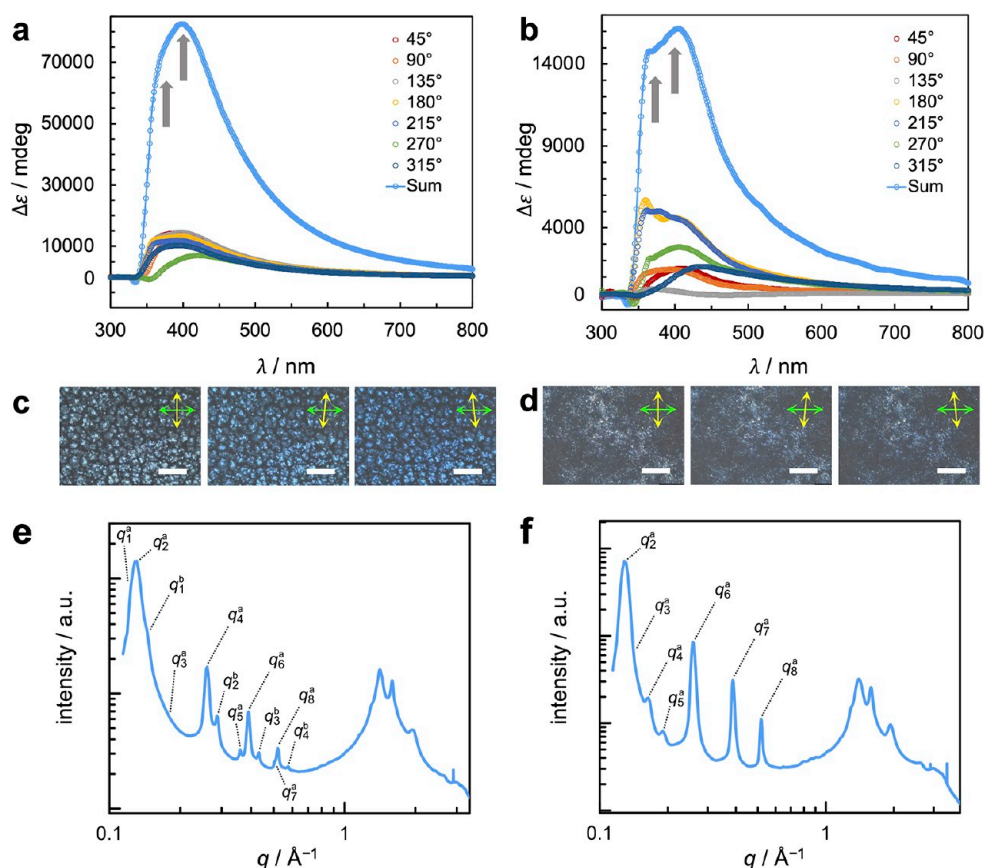
Figure 5. Thin-film CD spectra ($\Delta\varepsilon$ [mdeg] vs λ [nm]) of 10 μm films between untreated quartz substrates (compound **1**) after cooling at different cooling rates from the isotropic liquid phase to room temperature at different sample rotation angles, as indicated in the plot: (a) upon slow cooling (5 °C min^{-1}) and (b) upon rapid cooling ($\geq$50 °C min^{-1}). The shoulder at λ = 370 nm and the main peak at λ = 410 nm are highlighted by gray arrows. POM images of the 10 μm CD samples between quartz slides with crossed and decrossed polarizer and analyzer upon (c) slow cooling and (d) rapid cooling. The scale bar = 100 μm. Synchrotron XRD analysis data (compound **1**) taken at room temperature (T = 20 °C) showing intensity (au) vs wave vector q (Å^{-1}) upon: (e) slow cooling (see also Figure S14,b) and (f) fast cooling (see also Figure S14c).

dimensions of the HNFs like HNF$_{mod2b}$; dimensions that have previously only been observed for compound **III**[20] with an opposite configuration of the chiral centers in each side chain [(R,S) and (S,R)]. The other observed morphology is nanocylinders (NCs); some of which show a hint of helicoidal layering in the SEM images as previously observed 80 nm in diameter HLNC for compound **V**[25], however, a clear handedness is not visible here. This is perhaps less puzzling given that the (S,S)-2,3-difluorooctyloxy group induces a change from the linear projection of the aliphatic chain relative to the adjacent biphenyl cores to a more bent projection. Since this occurs in the meta- and the para-arms, the added conformational rigidity imparted by the *gauche* effect also favors the formation of nanofilaments with a cylindrical curvature. The dimensions of these cylindrical filaments range from about 40−80 nm and do not appear to be hollow (no gradient intensity across the filaments in TEM), thus indicating that about 5−10 layers are coaxially rolled up when forming the NC morphology in analogy to compound **V**. Such a decrease in NC diameter appears to be related to the increasing length of the aliphatic side chain from a branched C7 for **V** to a non-branched C8 for **1**, which has previously been observed for (HL)NC formed by a homologue of compound **V** with C10 aliphatic chains (the NC with no visible helicoidal layering in this case showed diameters of ∼60

nm).[26] The TEM images (Figure 3g,h) are in agreement with the SEM observations.

Imaging data collected upon rapid cooling from the isotropic liquid phase (≥50 °C min^{-1}) did not show any significant differences to those recorded upon slow cooling. The bluish textures appeared less defined, showing no specific features but a grainy appearance, but otherwise all the same features with respect to the texture seen when toggling the relative positions of the decrossed polarizer and analyzer (Figure 4a−d). DSC shows again only one phase transition on heating and cooling at a rate of 50 °C min^{-1} and a slightly broader phase transition (Figure S10b and Table S1). Less defined again due to the rapid thermal quench, both SEM and TEM images (Figure 4e−h) show the coexistence of the same two morphologies, larger-width HNFs and NCs, with some areas showing twisted bamboo-like structures that could be interpreted as a merger of the two more distinct morphologies seen upon slow cooling (see TEM image in Figure 4h and Supporting Information, Figure S13). The NC filaments are all somewhat shorter than those seen upon slow cooling, which is expected given the much faster kinetics of nucleation upon such rapid cooling. Overall, however, all microscopy images collected upon slow and rapid cooling indicate the formation of a B4 phase with a coexistence of two filament morphologies driven by the position and nature of the chiral centers in **1**[23] and the ensuing conformational rigidity of the two aliphatic side chains. To
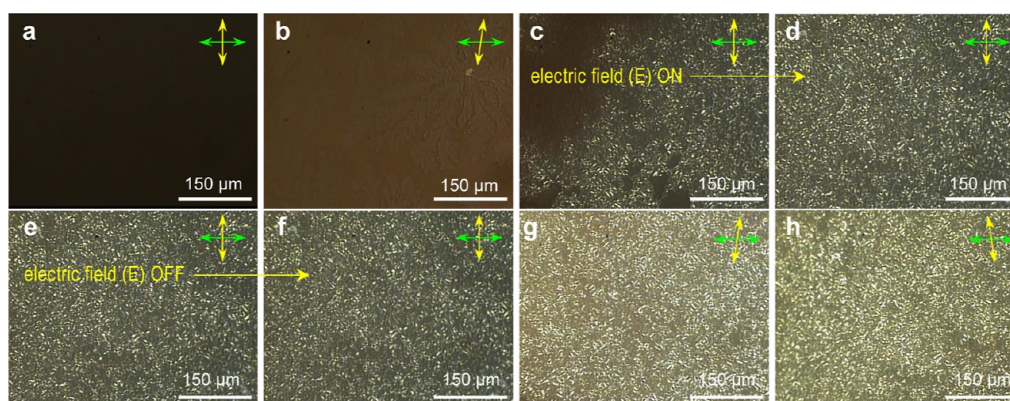
Figure 6. Polarized optical photomicrographs (compound **1**) of 6 μm thin films between ITO-coated glass after heating to the isotropic liquid phase (>175 °C) and subsequent slow cooling to room temperature (~20 °C) at a rate of 5 °C min^{-1}: (a) isotropic liquid phase (crossed polarizers) at T = 178 °C, (b) the just forming B4 phase showing the aforementioned characteristic features at T = 165 °C with decrossed polarizers and analyzers (+8°), (c) after starting to apply a triangular wave voltage of 10 V μm^{-1} (1 Hz) at T = 160 °C, a characteristic stripe grainy texture starts to form and (d) is completely formed after a time of t = 30 s. (e) After field removal, this texture persists (f) after 24 h and beyond. (g,h) the same texture shown in (f) after toggling the decrossed polarizer and analyzer orientation by ±8°.
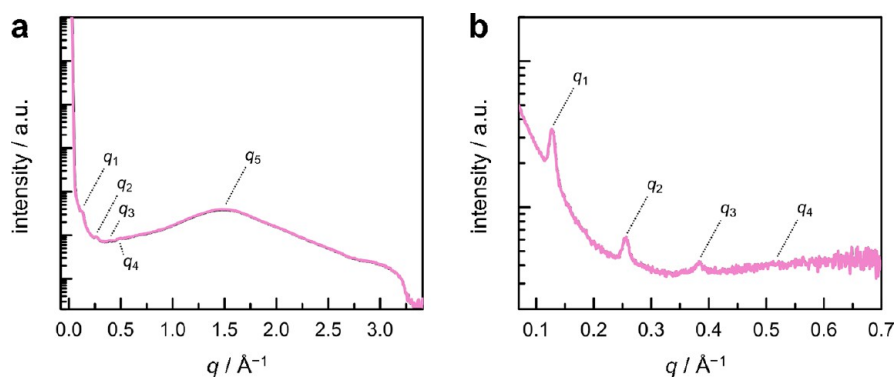
Figure 7. XRD analysis data (compound **1**) showing intensity (au) vs wave vector q (Å^{-1}) of compound **1** after applying at electric field on cooling from the isotropic liquid phase: (a) high-resolution medium-angle and (b) high-resolution small-angle region. To acquire the data, the sample was removed from the ITO cells by breaking the cell open and transferring the material to a capillary.

further examine these morphologies, we next performed thin-film CD and XRD experiments.

Considering the left-handed HNFs seen by EM on both slow and rapid cooling as well as the trend based on the (S)-configuration of the two chiral centers at C2 in each side chain for compound **1**, the thin film CD plots then show the anticipated positive sum-CD signals (Figure 5a,b). The two pronounced maxima seen in the sum CD spectra (peak at λ = 410 nm and shoulder at λ = 370 nm) correlate to the two morphologies seen by EM imaging; the shoulder peak corresponds to the HNFs as for compounds **II** and **III**,[20,23] and the peak at λ = 410 nm corresponds to the NCs as assigned previously for compound **VI**.[25] POM images taken for the 10 μm films between quartz substrates share the same features of the POM images shown for **1** earlier (Figure 5c,d).

To fully characterize the structures of the B4 phases (morphologies) formed by compound **1** on rapid or slow cooling, we performed synchrotron XRD experiments (see Materials and Methods Section for more details). Summaries of the obtained XRD data are shown in Figure 5e,f (small angle regions and deconvolution data are provided in the Supporting Information, Figure S14). On slow cooling from the isotropic liquid phase (Figure 5e), **1** shows two sets of diffraction peaks labeled $q_1^a - q_8^a$ and $q_1^b - q_4^b$ that correlate to the two B4 morphologies seen by EM imaging. Considering peak

assignments made for the corresponding morphologies formed by compounds **II**, **III**, and **VI**, the peak assignment for the q_x^a series matches a dual modulated HNF structure with the larger dimensions seen by EM imaging (HNF$_{mod2b}$) with q_1^a = 0.124 Å^{-1}, q_2^a = 0.129 Å^{-1} (corresponding to a d-spacing of 48.7 Å matching the length of the molecule l = 48.5 Å), $q_3^a = \sqrt{q_1^{a2} + q_2^{a2}}$ = 0.179 Å^{-1}, $q_4^a = 2q_2^a$ = 0.261 Å^{-1}, $q_5^a = 2q_3^a$ = 0.359 Å^{-1}, $q_6^a = 3q_2^a$ = 0.387 Å^{-1}, $q_7^a = 4q_1^a$ = 0.505 Å^{-1}, and $q_8^a = 4q_2^a$ = 0.515 Å^{-1}. The second set of peaks, q_x^b, is then best indexed as (001), (002), (003), and (004), suggesting a non-modulated layer structure with q_1^b = 0.144 Å^{-1}, indicating tilted molecules (θ = 26°), $q_2^b = 2q_1^b$ = 0.287 Å^{-1}, $q_3^b = 3q_1^b$ = 0.432 Å^{-1}, and $q_4^b = 4q_1^b$ = 0.576 Å^{-1}. Upon rapid cooling (Figure 5f), however, and in contrast to the EM results, only one dual modulated structure was seen, which is likely due to the X-ray catching a domain with predominantly one of the morphologies (here the HNF$_{mod2b}$) based on the close matching peak positions with q_1^a = 0.100 Å^{-1} (not in scale, but calculated from the correlated modulation peaks), q_2^a = 0.129 Å^{-1} (corresponding to a d-spacing of 48.7 Å matching the length of the molecule l = 48.5 Å), q_3^a = 0.140 Å^{-1}, $q_4^a = \sqrt{q_1^{a2} + q_2^{a2}}$ = 0.163 Å^{-1}, $q_5^a = \sqrt{q_2^{a2} + q_3^{a2}}$ = 0.190 Å^{-1}, $q_6^a = 2q_2^a$ = 0.258 Å^{-1}, $q_7^a = 3q_2^a$ = 0.388 Å^{-1}, and $q_8^a = 4q_2^a$ = 0.519 Å^{-1}. With the structures solved, the next step was to test
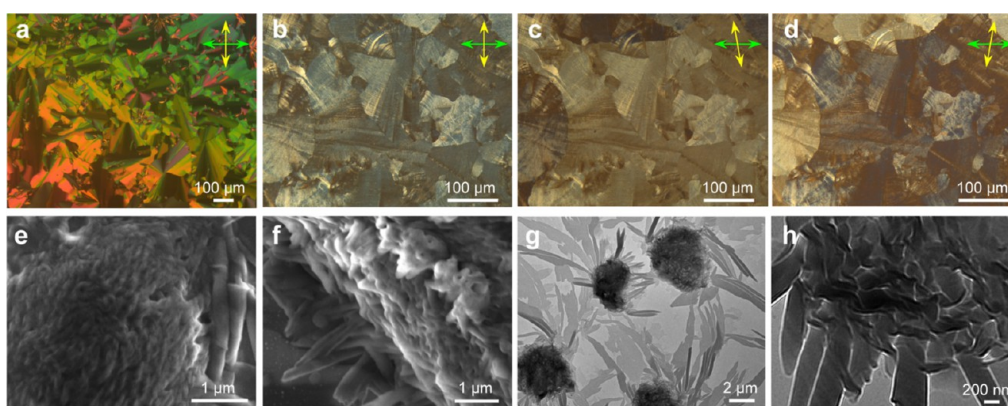
Figure 8. Polarized optical photomicrographs (compound **2**) after heating to the isotropic liquid phase (>175 °C) and subsequent slow cooling to room temperature (∼20 °C) at the cooling rate of 5 °C min^{-1}: (a) crossed polarizers at $T = 173$ °C, (b) crossed polarizers at $T = 90$ °C and (c,d) ± 10° decrossed polarizers at $T = 90$ °C. (e,f) SEM images (different domains) after heating to the isotropic liquid phase, followed by slow cooling to room temperature. (g,h) TEM images obtained upon slow cooling (different representative areas on the grid).

how compound **1** responds to an electric field applied right at the phase transition from the isotropic liquid to the B4 phase on slow and fast cooling.

Figure 6 shows the POM images for compound **1** just before (still in the isotropic liquid state, Figure 6a), during, and after applying the electric field (triangular wave, 1 Hz, up to 10 V μm^{-1}). Right at the phase transition (Figure 6b), the typical features of the B4 phase are clearly visible, but immediately upon applying an electric field, the appearance of the texture rapidly changes and evolves (Figure 6c,d) to a typical striped grainy texture commonly observed for the SmC$_A$P$_A$ texture — one of the B2 phases (Figure 6e−h) — once the electric field is turned off, as reported by several other groups.[67,72] Practically the exact same textures also form when this temperature and applied electric field protocol is reproduced at higher rates of cooling (for images at 20 °C min^{-1}, see Supporting Information, Figure S15). Phase transition temperatures shown in Figure 1 are here from POM since DSC data acquisition with an applied electric field was not possible. Furthermore, the blue structural color, otherwise characteristic of a B4 phase, was no longer observed for this electric field-treated sample of compound **1** in reflection.

XRD experiments were performed to support the microscopy findings and examine the exact structure of compound **1** after applying an electric field. The obtained diffraction patterns clearly deviate from those recorded earlier for the B4 morphologies. Instead, a simple smectic diffraction pattern with $q_1 = 0.13$ Å^{-1} (corresponding to $d = 48.3$ Å and thus a low tilt of $\theta = 8.5°$) $q_2 = 2q_1 = 0.26$ Å^{-1}, $q_3 = 3q_1 = 0.39$ Å^{-1}, a weak scattering maximum at $q_4 = 4q_1 = 0.52$ Å^{-1}, and a wide-angle broad, diffuse scattering q_5 (centered at $q = 1.5$ Å$^-$) was recorded (Figure 7). The latter precludes a B4 structure, for which the diffraction pattern in the q-range corresponding to lateral molecular distances shows multiple sharper peaks due to the crystalline nature within B4 filaments.[77] Thus, XRD and POM confirm the formation of a simple layered structure under these conditions, thus strongly suggesting the formation of a SmC$_A$P$_A$ or SmC$_S$P$_A$ B2 texture.

3.2. Compound 2 with an Azobenzene Para-Arm

Armed with the knowledge that an applied electric field as an external stimulus can alter the phase structure of a BC-LC with suitably responsive molecular motives, **2** underwent the same

experimental protocol, now tracing its behavior before and after irradiation with UV light.

At a slow rate of temperature change (5 °C min^{-1}), DSC shows one phase transition on heating and two phase transitions on cooling for compound **2** (Figure S16a and Table S2). POM confirms these results by showing what is sometimes described as a banana leaf-like texture[72] at higher temperatures on cooling from the isotropic liquid (Figure 8a), followed by a phase transition that is characterized by noticeable changes to a low birefringence texture with mosaic and spherulitic domains that show the characteristic swap between dark and bright domains as one toggles the orientation of decrossed polarizers and analyzers (Figure 8b−d and Supporting Information, Figure S17). These exact textural traits are shared among B4 phases formed by achiral bent-core molecules, thereby indicating the formation of a conglomerate of coexisting and adjacent homochiral domains[18] formed by filaments with opposite handedness that grow, chirality-preserving, with equal probability.[78] SEM and TEM imaging support the formation of nanofilaments upon slow cooling, showing just like for **1** a coexistence of two morphologies in a similar form of mixed crystals. The HNFs seen in Figure 8e,f show dimensions of $w \sim 100$ nm and a helical pitch of $p \sim 350$ nm like the HNF$_{mod2b}$ formed by compound **1** and as reported earlier by compound **III**.[20] The handedness of the domain in Figure 8e is left-handed, but other domains show the opposite handedness (Supporting Information, Figure S18). The other clearly distinct morphology is HLNC,[25] where a left-handed helicoidal wrapping is clearly visible (Figure 8f); possibly by chance, helicoidal layering with the opposite handedness was not seen in any of the SEM images.[26] The average diameter of the HLNCs ranges from 250−300 nm, which would translate to 25−30 layers (given the molecular length of compound **2** of $l = 51$ Å). TEM images further supported the coexistence of two morphologies as mixed crystals, often showing a core of bundled HNFs from which NCs appeared to spread outward (Figure 8g,h). The HLNCs formed are now significantly larger than those seen for compound **1**.

Microscopic studies performed for **2** upon rapid cooling largely echo those obtained after slow cooling from the isotropic liquid. POM textures after the rapid thermal quench show a less defined grainy, bluish mosaic appearance characterized by smaller domains (as expected for rapid
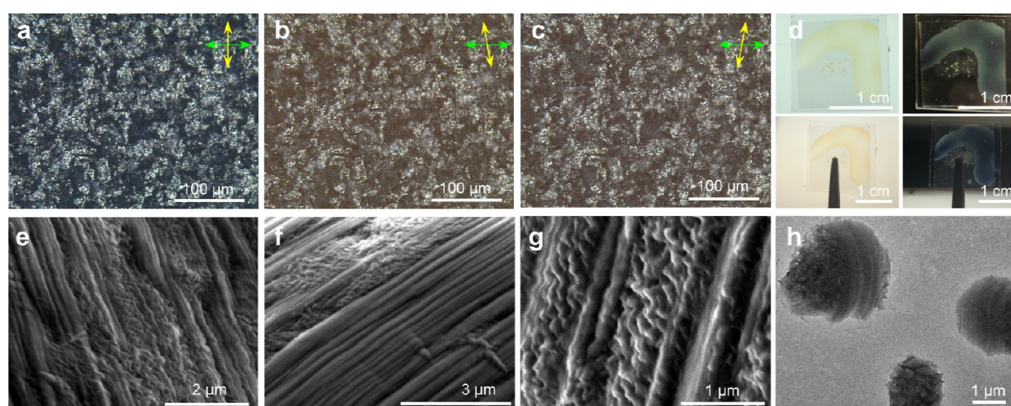
Figure 9. Polarized optical photomicrographs (compound **2**) after heating to the isotropic liquid phase (>175 °C) and subsequent rapid cooling to room temperature (~20 °C) at the cooling rate of ≥50 °C min^{-1}: (a) crossed polarizers at T = 20 °C as well as (bc) ±10° decrossed polarizers at T = 20 °C. (d) Sample photographs showing the B4 typical yellow color in transmission and blue structural color in reflection (top row: on a backlight illuminated and then a dark surface; bottom row: held up against a light or dark background with the latter image clearly showing the blue structural color). (e−g) SEM images after heating to the isotropic liquid phase followed by rapid cooling to room temperature (different domains). (h) Representative TEM image obtained upon rapid cooling.
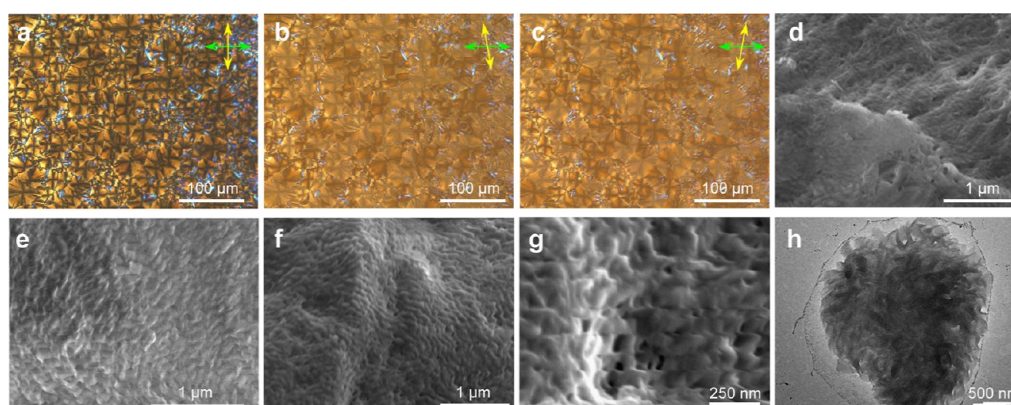

Figure 10. Polarized optical photomicrographs (compound **2**) after heating to the isotropic liquid phase (>175 °C) and subsequent slow cooling to room temperature (~20 °C) at the cooling rate of 5 °C min^{-1} with UV irradiation at λ = 365 nm: (a) crossed polarizers at T = 20 °C as well as (b) and (c) ±10° decrossed polarizers at T = 20 °C. (d,e) SEM images after UV irradiation heating to the isotropic liquid phase, followed by slow cooling to room temperature (different domains and magnification). (f,g) SEM images after UV irradiation and after heating to the isotropic liquid phase followed by rapid cooling to room temperature (different domains and magnification). (h) Representative TEM image obtained upon slow cooling after UV irradiation.

cooling), which again show alternating darker and lighter subdomains when the orientation of the decrossed polarizer and analyzer is toggled (Figure 9a−c and Supporting Information, Figure S19). Sample photographs show the well-documented yellow color in transmission and a blue structural color in reflection (Figure 9d). SEM images continue to show coexistence of the same two morphologies with almost identical dimensions as those seen on slow cooling (Figure 9e−g). Here, HNFs with either handedness can be seen (see Supporting Information, Figure S20) due to the smaller domain size, but any helicoidal layering in these images is difficult to make out. Perhaps a right-handed layering can be seen in the one filament that grew perpendicular to the other longer filaments (bottom right in Figure 9f). TEM images then show clusters of HNFs that appear wrapped in smooth cylinder-like structures (Figure 9h).

Continuous irradiation of a sample of **2** initially dissolved in an organic solvent (CH$_2$Cl$_2$) and during complete solvent evaporation and heating to the isotropic liquid to generate a thin film with UV light at λ = 365 nm then generated some marked differences in all the microscopy images upon cooling.

Lacking a photo-DSC setup, determination of the phase transition temperatures for the UV-irradiated sample of compound **2** was accomplished by POM. With respect to the textural observations, the rate of cooling had absolutely no impact here, and all images recorded under either cooling rate were practically identical. In POM, the orange and blue textures with focal conic domains that appeared showed again the typical alternating darker and lighter domains when toggling the analyzer position away from the 90° crossed polarizer position (Figure 10a−c). Similar, yet singularly blue textures were previously reported for parent compounds **II** and **III**[23] on slow and rapid cooling, as well as for compound **VI** on rapid cooling only. In all prior cases, such a texture was formed by HNF morphologies without any coexistence of other morphologies. SEM imaging further supports this, showing only one B4 morphology and no coexistent second morphology (Figure 10e−g). All images show solely HNFs with random left or right handedness and similar dimensions as those seen during cooling without UV irradiation (average width of w = 100 nm and pitch of p = 250−300 nm). We attribute this to the initially considered Weigert effect, where
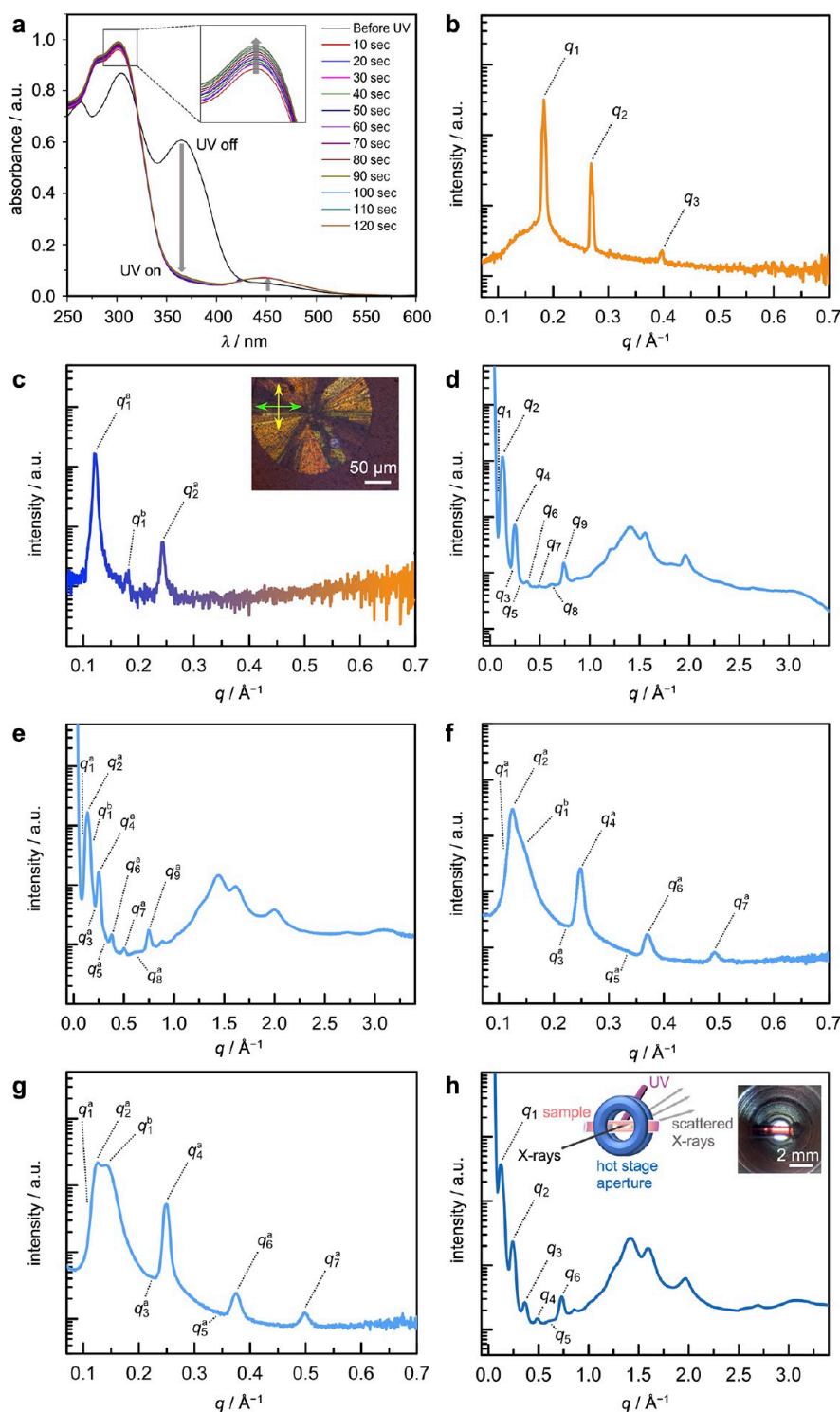
Figure 11. (a) UV−vis spectra recorded for compound **2** prior to and during UV irradiation at λ = 365 nm. (b)−(h) XRD analysis data for compound **2** showing intensity (au) vs wave vector q (Å^{-1}): (b) high-temperature phase upon slow cooling at T = 165 °C (c) between Kapton windows on slow cooling at T = 157 °C right at the transition from the high to the low temperature phase (inset shows the in vacuo POM image of the evolving spherulitic domain of the B4 phase taken inside the SAXS instrument sample chamber), (d) low-temperature phase on slow cooling at T = 90 °C, (e)−(f) low-temperature phase upon rapid cooling (thermal quench): (e) survey scan, (f,g) two different sample spots in capillary, and (h) in a capillary under continued in situ UV light (λ = 365 nm) irradiation (insert shows the experimental setup both as a schematic at the bottom and in a photograph at the top right taken with the camera that points exactly at the sample location interrogated by the X-rays). Deconvolutions of low-q signals are provided in the Supporting Information (Figures S25 and S26).

continued exposure to UV irradiation and fast thermal back relaxation to the cis-isomer leads to an equilibrium that lies on the side of the thermodynamically more stable trans-isomer of

the azobenzene situated in the para-arm. This process then aligns the molecules along the path of light irradiation, as demonstrated by Yoon et al. for BC-LCs based on azobenzene

dimers connected by a flexible aliphatic tether.[27,28] As a consequence, the UV irradiation favors the formation of HNFs over (HL)NCs, where UV light alignment and coaxial layering, if the orientation of the molecular bend is parallel to the long axis of the NC filaments, would impede helicoidal wrapping. Again, TEM imaging then shows the clustered HNFs without the previously seen wrapping by the other morphology (Figure 10h).

Photophysical and XRD experiments were used to better understand the behavior of **2** and to fully examine the structures formed under the various experimental conditions. UV−vis spectra recorded prior to and during UV irradiation (at $\lambda = 365$ nm; over 2 min in 10 s intervals) show that the trans-configuration of the azobenzene in **2** rapidly isomerizes to the cis-configuration (Figure 11a). A deconvolution of the UV−vis spectrum prior to UV irradiation (Supporting Information, Figure S21) shows that 9% of **2** are already in the cis-configuration, likely the thermodynamic equilibrium, as practically identical UV−vis spectra were acquired from thin films of **2** with and without the UV-exposure but following the same thermal treatment (Supporting Information, Figure S22).

On slow cooling from the isotropic liquid (Figure 11b and Supporting Information, Figure S23), the high-temperature phase formed by **2** shows three diffraction peaks labeled q_1−q_3 at $q_1 = 0.183$ Å^{-1}, $q_2 = 0.269$ Å^{-1}, and $q_3 = 0.395$ Å^{-1}, indexed as (11), (02), and (31) with a two-dimensional rectangular lattice (plane group $c2mm$) and lattice parameters of $a = 46.7$ Å, and $c = 50.6$ Å (note that the molecular length of **2** is $l = 51.1$ Å); a phase that is also formed by parent compound **I** on heating and cooling[23] as well as compound **V**[25] on rapid cooling. At the phase transition to the low-temperature phase (imaged and pinpointed by the in vacuo POM insert within the SAXS sample chamber; for the setup, see Supporting Information, Figure S24), a remnant peak from the Col_r−$c2mm$ phase at $q_1^b = 0.183$ Å^{-1} and two emerging new maxima at $q_1^a = 0.122$ Å^{-1} and $q_2^a = 2q_1^a = 0.244$ Å^{-1} from the originating B4 phase were recorded (Figure 11c). On further slow cooling below the phase transition, **2** shows a set of diffraction peaks labeled q_1−q_9 with $q_1 = 0.112$ Å^{-1}, $q_2 = 0.122$ Å^{-1}, ($d = 51.5$ Å, matching the molecular length of **2**), $q_3 = 2q_1 = 0.223$ Å^{-1}, $q_4 = 2q_2 = 0.244$ Å^{-1}, $q_5 = 3q_1 = 0.343$ Å^{-1}, $q_6 = 3q_2 = 0.367$ Å^{-1}, $q_7 = 4q_2 = 0.488$ Å^{-1}, $q_8 = 5q_2 = 0.611$ Å^{-1}, and $q_9 = 6q_2 = 0.734$ Å^{-1}, and thus a highly ordered, likely intralayer-modulated layer structure (based on the additional correlated diffraction peaks at q_1, q_3, and q_5) in these filaments (Figure 11d, and Supporting Information, Figure S25 for a better resolution plot at lower q). Given the dimensions seen by EM imaging, this would then translate to a HNF$_{modb}$ morphology (with the subscript "b" simply indicating the larger physical dimensions of the modulated HNFs). A separate set of diffraction peaks belonging to the second B4 morphology seen by EM imaging, however, was not detected by XRD on slow cooling (even by probing various sample locations), which could occur if both morphologies are non-tilted, as indicated by the calculated layer spacing (d) for the HNF$_{modb}$ morphology.

This situation changes on rapid cooling, where just like in the SEM and TEM images, two distinct morphologies can be identified by analyzing the XRD pattern (Figure 11e−g, and Supporting Information, Figure S26 for deconvolutions of the low q signals). Here, **2** shows two sets of diffraction peaks with varying intensity depending on the sample location interrogated along the capillary, labeled q_1^a−q_9^a and a single peak without any correlation to the q_x^a set, $q_1^b = 0.141$ Å^{-1},

corresponding to $d = 44.6$ Å (i.e., a layer structure with a tilt of $\theta = 29°$). For the q_x^a set itself, $q_1^a = 0.110$ Å^{-1}, $q_2^a = 0.123$ Å^{-1} (corresponding to a d-spacing of 51.1 Å matching the length of the molecule $l = 51.1$ Å), $q_3^a = 2q_1^a = 0.221$ Å^{-1}, $q_4^a = 2q_2^a = 0.246$ Å^{-1}, $q_5^a = 3q_1^a = 0.331$ Å^{-1}, $q_6^a = 3q_2^a = 0.396$ Å^{-1}, $q_7^a = 4q_2^a = 0.492$ Å^{-1}, $q_8^a = 5q_2^a = 0.615$ Å^{-1}, and $q_9^a = 6q_2^a = 0.738$ Å^{-1}, similar to the modulated B4 morphology with no layer tilt already found on slow cooling, but now with a different intralayer modulation (i.e., HNF$_{mod'b}$). The clear identification of the second morphology, the (HL)NC, may here be aided by the overall smaller domain size, as seen by EM imaging, which as expected given the rapid thermal quench now intermix more readily and are more simultaneously captured by the interrogating X-ray beam. In such a situation, the intensity of the two major diffraction peaks (q_2^a and q_1^b), each correlated to the layer spacing, occurs at almost equal intensities (as seen in Figure 11g).

Finally, we devised an experimental setup where a sample of **2** in a capillary that was prepared exactly as the samples studied by POM and EM is further irradiated with UV light in situ during data collection within the evacuated sample chamber at the phase transition. Figure 11h shows the diffraction pattern at exposure to UV light at $\lambda = 365$ nm. Six clearly discernible diffraction peaks, with $q_1 = 0.123$ Å^{-1} ($d = 51.1$ Å, again matching the molecular length of **2**), $q_2 = 2q_1 = 0.247$ Å^{-1}, $q_3 = 3q_1 = 0.370$ Å^{-1}, $q_4 = 4q_1 = 0.493$ Å^{-1}, $q_5 = 5q_1 = 0.615$ Å^{-1}, and $q_6 = 6q_1 = 0.732$ Å^{-1} (see Supporting Information, Figure S27a, for a plot of the small angle region) further suggest the sole existence of only one of the previous two B4 morphologies, i.e., a non-tilted B4 HNF$_b$ morphology (based on the first diffraction peak, q_1), as hinted at by POM and confirmed by EM imaging (see Figure 10). Thus, in the case of compound **2**, the UV exposure protocol serves as a selector for one of the two morphologies previously formed in coexistence with one another without irradiation at $\lambda = 365$ nm. Considering the inherent radial molecular orientation of the BC-LC molecules established for the nanocylinder morphology, which seems noncommensurate with the active UV light alignment mechanism previously described by Yoon and co-workers,[27,28] the morphology that does allow for the alignment of the BC-LC molecules along the path of irradiation, the HNF morphology, becomes the prevailing morphology. Furthermore, UV light-promoted alignment also negates the intralayer modulation seen prior to UV irradiation (Supporting Information, Figure S27b), producing the non-modulated HNF$_b$ morphology.

4. CONCLUSIONS

The exceptional ability of molecules with a bent molecular shape to form hierarchically self-assembled nanoscale building blocks in the form of flat ribbons, helical filaments with negative Gaussian, or layered nanocylinders with a cylindrical curvature—so-called B4 phases—has quickly transformed these molecules into desirable building blocks for a variety of potential applications in optics,[79,80] energy harvesting,[81] chirality transfer,[82] or as templates[21,83,84] for circularly polarized emission using aggregation-induced emission dyes.[85,86]

While we have previously shown that these nanoscale organic building blocks can, to some degree, be logically blended to obtain a specific filament type with a priori-predicted handedness,[87] actively changing the phase from B4 to another phase or guiding the formation of only one select
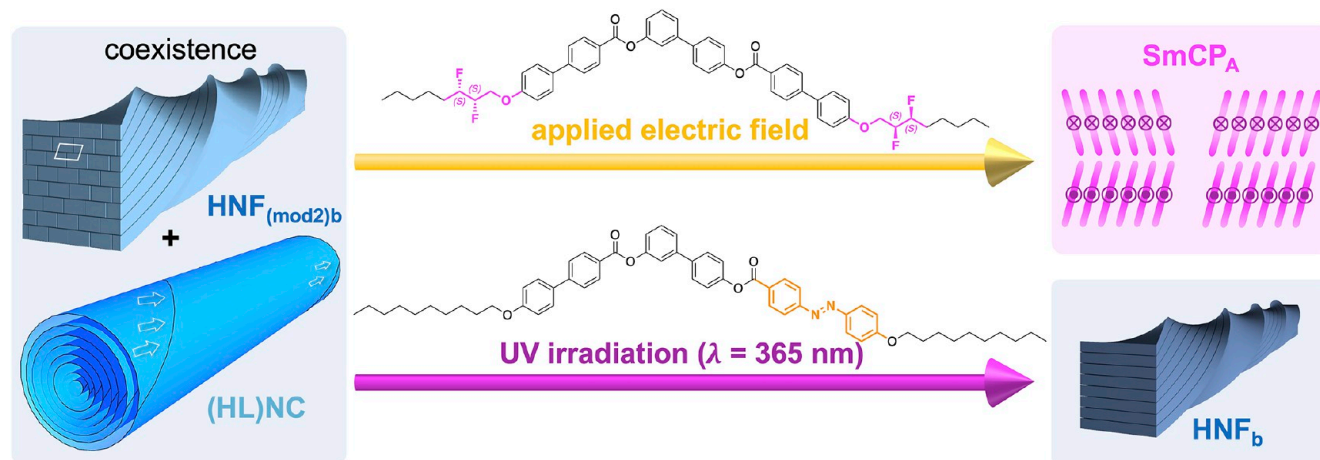
Figure 12. Graphical summary of the response of compounds **1** and **2** to applied external stimuli in addition to thermal control by adjusting the cooling rate from the isotropic liquid phase.

B4 morphology using external stimuli has not been realized. The current work demonstrates that deliberate molecular design within the parameter space of bent-core molecules that can form the B4 phase allows for either phase or morphological control using external stimuli such as applied electric fields or UV irradiation. While the parent molecules lacking structural motifs such as conformationally rigid SPUs or photoactive azobenzenes permitted structural or morphological changes only in response to variations in the cooling rate from the isotropic liquid phase (i.e., thermal control or trigger), the approach detailed here adds two additional external trigger modes to select either a specific phase (from a B4 crystalline to a B2 liquid crystalline phase[88]) or to gradually eliminate the coexistence of one of two morphologies in favor of the one that is more commensurate to the photoalignment of the azobenzene-containing molecules along the path of irradiation[27,28] (see the graphical summary in Figure 12).

The morphology coexistence observed for either molecule prior to exposure to the respective external stimulus likely finds its origin in the kinetics of formation (and nucleation) of the nanofilaments[78] depending on the rate of cooling, but requires further, more in-depth studies by gradually adjusting the rate of cooling at much smaller intervals than chosen thus far. Such experimental studies are underway and will be reported in due course. Combined with the templating ability of B4 nanofilaments, triggering a phase or morphology change by external stimuli, as shown here, will also permit some degree of external control over the properties (circularly polarized emissive, for example) of any helical or helicoidal assembled guests, leading to potential applications.

ASSOCIATED CONTENT

ⓈⒾ Supporting Information

The Supporting Information is available free of charge at https://pubs.acs.org/doi/10.1021/acsnanoscienceau.3c00005.

> Details of syntheses and all analytical data (^{1}H, ^{13}C, and ^{19}F NMR, MS, and elemental analysis) of compounds **1** and **2**; additional DSC plots and data, POM, SEM, and TEM images, and XRD data (PDF)

AUTHOR INFORMATION

Corresponding Authors

Marianne E. Prévôt − *Advanced Materials and Liquid Crystal Institute, Kent State University, Kent, Ohio 44242, United States*; Email: mprevot1@kent.edu

Torsten Hegmann − *Advanced Materials and Liquid Crystal Institute, Kent State University, Kent, Ohio 44242, United States; Materials Science Graduate Program, Department of Chemistry and Biochemistry, and Brain Health Research Institute, Kent State University, Kent, Ohio 44242, United States*; ⓘ orcid.org/0000-0002-6664-6598; Email: thegmann@kent.edu

Authors

Barış Sezgin − *Department of Chemistry, Süleyman Demirel University, 32260 Isparta, Turkey; Advanced Materials and Liquid Crystal Institute, Kent State University, Kent, Ohio 44242, United States*; ⓘ orcid.org/0000-0001-5359-4488

Jiao Liu − *Advanced Materials and Liquid Crystal Institute, Kent State University, Kent, Ohio 44242, United States; Materials Science Graduate Program, Kent State University, Kent, Ohio 44242, United States*

Diana P. N. Gonçalves − *Advanced Materials and Liquid Crystal Institute, Kent State University, Kent, Ohio 44242, United States; Department of Chemistry and Biochemistry, Kent State University, Kent, Ohio 44242, United States*

Chenhui Zhu − *Advanced Light Source, Lawrence Berkeley National Laboratory, Berkeley, California 94720, United States*

Tahir Tilki − *Department of Chemistry, Süleyman Demirel University, 32260 Isparta, Turkey*

Complete contact information is available at:
https://pubs.acs.org/10.1021/acsnanoscienceau.3c00005

Author Contributions

T.H., B.S., and J.L. conceived the described experiments. T.T. supervised the synthesis of the azobenzene precursor. J.L. and B.S with the help of D.P.N.G. performed the syntheses and analytical characterization of the materials. J.L. and B.S. did the POM, SEM, and TEM studies, J.L. did CD, and M.E.P as well as C.Z. performed all the XRD studies. T.H. directed the research and wrote the manuscript with contributions from all

Notes

■ ACKNOWLEDGMENTS

■ REFERENCES

(1) Bhushan, B. Biomimetics: Lessons from Nature-An Overview. *Philos. Trans.: Math., Phys. Eng. Sci.* **2009**, *367*, 1445−1486.

(2) Teyssier, J.; Saenko, S. V.; van der Marel, D.; Milinkovitch, M. C. Photonic Crystals Cause Active Colour Change in Chameleons. *Nat. Commun.* **2015**, *6*, 6368.

(3) Mathger, L. M.; Hanlon, R. T. Anatomical basis for camouflaged Polarized Light Communication in Squid. *Biol. Lett.* **2006**, *2*, 494−496.

(4) White, J.; Yamashita, F. Boquila Trifoliolata Mimics Leaves of an Artificial Plastic Host Plant. *Plant Signal. Behav.* **2022**, *17*, 1977530.

(5) Merg, A. D.; Touponse, G.; Genderen, E. v.; Blum, T. B.; Zuo, X. B.; Bazrafshan, A.; Siaw, H. M. H.; McCanna, A.; Brian Dyer, R.; Salaita, K.; Abrahams, J. P.; Conticello, V. P. Shape-Shifting Peptide Nanomaterials: Surface Asymmetry Enables pH-Dependent Formation and Interconversion of Collagen Tubes and Sheets. *J. Am. Chem. Soc.* **2020**, *142*, 19956−19968.

(6) Gosecki, M.; Zgardzinska, B.; Gosecka, M. Temperature-Induced Changes in the Nanostructure of Hydrogels Based on Reversibly Cross-Linked Hyperbranched Polyglycidol with $B(OH)_4^{\ominus}$ Ions. *J. Phys. Chem. C* **2016**, *120*, 18323−18332.

(7) Rehn, S. M.; Gerrard-Anderson, T. M.; Qiao, L.; Zhu, Q.; Wehmeyer, G.; Jones, M. R. Mechanical Reshaping of Inorganic Nanostructures with Weak Nanoscale Forces. *Nano Lett.* **2021**, *21*, 130−135.

(8) Cabie, M.; Giorgio, S.; Henry, C. R.; Axet, M. R.; Philippot, K.; Chaudret, B. Direct Observation of the Reversible Changes of the Morphology of Pt Nanoparticles under Gas Environment. *J. Phys. Chem. C* **2010**, *114*, 2160−2163.

(9) Hung, A. M.; Kazembeyki, M.; Hoover, C. G.; Fini, E. H. Evolution of Morphological and Nanomechanical Properties of Bitumen Thin Films as a Result of Compositional Changes Due to Ultraviolet Radiation. *ACS Sustain. Chem. Eng.* **2019**, *7*, 18005−18014.

(10) Martin, N.; Sharma, K. P.; Harniman, R. L.; Richardson, R. M.; Hutchings, R. J.; Alibhai, D.; Li, M.; Mann, S. Light-Induced Dynamic Shaping and self-division of Multipodal Polyelectrolyte-Surfactant Microarchitectures via Azobenzene Photomechanics. *Sci. Rep.* **2017**, *7*, 41327.

(11) Zhu, Z. C.; Senses, E.; Akcora, P.; Sukhishvili, S. A. Programmable Light-Controlled Shape Changes in Layered Polymer Nanocomposites. *ACS Nano* **2012**, *6*, 3152−3162.

(12) Li, L. S.; Cui, S. B.; Hu, A.; Zhang, W.; Li, Y. W.; Zhou, N. C.; Zhang, Z. B.; Zhu, X. L. Smart Azobenzene-Containing Tubular Polymersomes: fabrication and Multiple Morphological Tuning. *Chem. Commun.* **2020**, *56*, 6237−6240.

(13) Xu, B. B.; Qian, H. Y.; Lin, S. L. Self-Assembly and Photoinduced Spindle-Toroid Morphology Transition of Macromolecular Double-Brushes with Azobenzene Pendants. *ACS Macro Lett.* **2020**, *9*, 404−409.

(14) Vlahovska, P. M. Voltage-Morphology Coupling in Biomimetic Membranes: Dynamics of Giant Vesicles in Applied Electric Fields. *Soft Matter* **2015**, *11*, 7232−7236.

(15) Sahoo, S.; Bhandaru, N.; Mukherjee, R. Reversible Morphological Switching And Deformation Hysteresis in Electric Field Mediated Instability of Thin Elastic Films. *Soft Matter* **2019**, *15*, 3828−3834.

(16) Hesabizadeh, T.; Jebari, N.; Madouri, A.; Hallais, G.; Clark, T. E.; Behura, S. K.; Herth, E.; Guisbiers, G. Electric-Field-Induced Phase Change in Copper Oxide Nanostructures. *ACS Omega* **2021**, *6*, 33130−33140.

(17) Gonçalves, D. P. N.; Prévôt, M. E.; Ustunel, S.; Ogolla, T.; Nemati, A.; Shadpour, S.; Hegmann, T. Recent Progress at the Interface Between Nanomaterial Chirality and Liquid Crystals. *Liq. Cryst. Rev.* **2021**, *9*, 1−34.

(18) Hough, L. E.; Jung, H. T.; Kruerke, D.; Heberling, M. S.; Nakata, M.; Jones, C. D.; Chen, D.; Link, D. R.; Zasadzinski, J.; Heppke, G.; Rabe, J. P.; Stocker, W.; Korblova, E.; Walba, D. M.; Glaser, M. A.; Clark, N. A. Helical Nanofilament Phases. *Science* **2009**, *325*, 456−460.

(19) Tsai, E.; Richardson, J. M.; Korblova, E.; Nakata, M.; Chen, D.; Shen, Y. Q.; Shao, R. F.; Clark, N. A.; Walba, D. M. A Modulated Helical Nanofilament Phase. *Angew. Chem., Int. Ed.* **2013**, *52*, 5254−5257.

(20) Shadpour, S.; Nemati, A.; Salamończyk, M.; Prévôt, M. E.; Liu, J.; Boyd, N. J.; Wilson, M. R.; Zhu, C. H.; Hegmann, E.; Jákli, A. I.; Hegmann, T. Missing Link between Helical Nano- and Microfilaments in B4 Phase Bent-Core Liquid Crystals, and Deciphering which Chiral Center Controls the Filament Handedness. *Small* **2020**, *16*, 1905591.

(21) Shadpour, S.; Nemati, A.; Liu, J.; Hegmann, T. Directing the Handedness of Helical Nanofilaments Confined in Nanochannels Using Axially Chiral Binaphthyl Dopants. *ACS Appl. Mater. Interfaces* **2020**, *12*, 13456−13463.

(22) Li, L.; Salamończyk, M.; Shadpour, S.; Zhu, C. H.; Jákli, A.; Hegmann, T. An Unusual Type of Polymorphism in a Liquid Crystal. *Nat. Commun.* **2018**, *9*, 714.

(23) Li, L.; Salamończyk, M.; Jákli, A.; Hegmann, T. A Dual Modulated Homochiral Helical Nanofilament Phase with Local Columnar Ordering Formed by Bent Core Liquid Crystals: Effects of Molecular Chirality. *Small* **2016**, *12*, 3944−3955.

(24) Alaasar, M.; Prehm, M.; Tschierske, C. Helical Nano-crystallite (HNC) Phases: Chirality Synchronization of Achiral Bent-Core Mesogens in a New Type of Dark Conglomerates. *Chem.—Eur. J.* **2016**, *22*, 6583−6597.

(25) Shadpour, S.; Nemati, A.; Boyd, N. J.; Li, L.; Prévôt, M. E.; Wakerlin, S. L.; Vanegas, J. P.; Salamończyk, M.; Hegmann, E.; Zhu, C. H.; Wilson, M. R.; Jákli, A. I.; Hegmann, T. Heliconical-Layered Nanocylinders (HLNCs) - Hierarchical Self-Assembly in a Unique B4 Phase Liquid Crystal Morphology. *Mater. Horiz.* **2019**, *6*, 959−968.

(26) Liu, J.; Shadpour, S.; Prévôt, M. E.; Chirgwin, M.; Nemati, A.; Hegmann, E.; Lemieux, R. P.; Hegmann, T. Molecular Conformation of Bent-Core Molecules Affected by Chiral Side Chains Dictates Polymorphism and Chirality in Organic Nano- and Microfilaments. *ACS Nano* **2021**, *15*, 7249−7270.

(27) Park, W.; Ha, T.; Kim, T. T.; Zep, A.; Ahn, H.; Shin, T. J.; Sim, K. I.; Jung, T. S.; Kim, J. H.; Pociecha, D.; Gorecka, E.; Yoon, D. K. Directed Self-Assembly of a Helical Nanofilament Liquid Crystal Phase for Use as Structural Color Reflectors. *NPG Asia Mater.* **2019**, *11*, 45.

(28) Park, W.; Wolska, J. M.; Pociecha, D.; Gorecka, E.; Yoon, D. K. Direct Visualization of Optical Activity in Chiral Substances Using a Helical Nanofilament (B4) Liquid Crystal Phase. *Adv. Opt. Mater.* **2019**, *7*, 1901399.

(29) Sun, J. Y.; Bhushan, B.; Tong, J. Structural Coloration in Nature. *RSC Adv.* **2013**, *3*, 14862−14889.

(30) Lugger, S. J. D.; Ceamanos, L.; Mulder, D. J.; Sanchez-Somolinos, C.; Schenning, A. P. H. J. 4D Printing of Supramolecular Liquid Crystal Elastomer Actuators Fueled by Light. *Adv. Mater. Technol.* **2023**, *8*, 2201472.

(31) Liao, W.; Yang, Z. Q. 3D Printing Programmable Liquid Crystal Elastomer Soft Pneumatic Actuators. *Mater. Horiz.* **2023**, *10*, 576−584.

(32) van Oosten, C. L.; Bastiaansen, C. W. M.; Broer, D. J. Printed artificial cilia from liquid-crystal network actuators modularly driven by light. *Nat. Mater.* **2009**, *8*, 677−682.

(33) Wang, Y. C.; Yin, R.; Jin, L. S.; Liu, M. Z.; Gao, Y. C.; Raney, J.; Yang, S. 3D-Printed Photoresponsive Liquid Crystal Elastomer Composites for Free-Form Actuation. *Adv. Funct. Mater.* **2023**, *33*, 2210614.

(34) Gelebart, A. H.; Jan Mulder, D.; Varga, M.; Konya, A.; Vantomme, G.; Meijer, E. W.; Selinger, R. L. B.; Broer, D. J. Making waves in a photoactive polymer film. *Nature* **2017**, *546*, 632−636.

(35) Lee, K. M.; Koerner, H.; Vaia, R. A.; Bunning, T. J.; White, T. J. Light-activated shape memory of glassy, azobenzene liquid crystalline polymer networks. *Soft Matter* **2011**, *7*, 4318−4324.

(36) Zheng, X.; Jia, Y.; Chen, A. Azobenzene-Containing Liquid Crystalline Composites for Robust Ultraviolet Detectors Based on Conversion of Illuminance-Mechanical Stress-electric Signals. *Nat. Commun.* **2021**, *12*, 4875.

(37) Guo, Y. B.; Zhang, J. C.; Hu, W. Q.; Khan, M. T. A.; Sitti, M. Shape-Programmable Liquid Crystal Elastomer Structures with

Arbitrary Three-Dimensional Director Fields and Geometries. *Nat. Commun.* **2021**, *12*, 5936.

(38) Serak, S.; Tabiryan, N.; Vergara, R.; White, T. J.; Vaia, R. A.; Bunning, T. J. Liquid Crystalline Polymer Cantilever Oscillators Fueled by Light. *Soft Matter* **2010**, *6*, 779−783.

(39) White, T. J.; Broer, D. J. Programmable and adaptive mechanics with Liquid Crystal Polymer Networks and Elastomers. *Nat. Mater.* **2015**, *14*, 1087−1098.

(40) Ware, T. H.; McConney, M. E.; Wie, J. J.; Tondiglia, V. P.; White, T. J. Voxelated Liquid Crystal Elastomers. *Science* **2015**, *347*, 982−984.

(41) Camacho-Lopez, M.; Finkelmann, H.; Palffy-Muhoray, P.; Shelley, M. Fast Liquid-Crystal Elastomer Swims Into the Dark. *Nat. Mater.* **2004**, *3*, 307−310.

(42) Todorov, P.; Georgieva, S.; Peneva, P.; Tchekalarova, J. Spectral and Electrochemical Solvatochromic Investigations of Newly Synthesized Peptide-Based Chemosensor Bearing Azobenzene Side Chain Bio Photoswitch. *Dyes Pigm.* **2021**, *191*, 109348.

(43) Wu, D.; Dong, M. X.; Collins, C. V.; Babalhavaeji, A.; Woolley, G. A. A Red-Light Azobenzene Di-Maleimide Photoswitch: Pros and Cons. *Adv. Opt. Mater.* **2016**, *4*, 1402−1409.

(44) Deo, C.; Bogliotti, N.; Metivier, R.; Retailleau, P.; Xie, J. A Visible-Light-Triggered Conformational Diastereomer Photoswitch in a Bridged Azobenzene. *Chem.—Eur. J.* **2016**, *22*, 9092−9096.

(45) Doran, T. M.; Anderson, E. A.; Latchney, S. E.; Opanashuk, L. A.; Nilsson, B. L. Correction to An Azobenzene Photoswitch Sheds Light on Turn Nucleation in Amyloid-beta Self-Assembly. *ACS Chem. Neurosci.* **2012**, *3*, 336.

(46) Negi, A.; Kieffer, C.; Voisin-Chiret, A. S. Azobenzene Photoswitches in Proteolysis Targeting Chimeras: Photochemical Control Strategies and Therapeutic Benefits. *ChemistrySelect* **2022**, *7*, No. e202200981.

(47) Böckmann, M.; Doltsinis, N. L.; Marx, D. Unraveling a Chemically Enhanced Photoswitch: Bridged Azobenzene. *Angew. Chem., Int. Ed.* **2010**, *49*, 3382−3384.

(48) Cheng, H. B.; Zhang, S. C.; Bai, E. Y.; Cao, X. Q.; Wang, J. Q.; Qi, J.; Liu, J.; Zhao, J.; Zhang, L. Q.; Yoon, J. Y. Future-Oriented Advanced Diarylethene Photoswitches: From Molecular Design to Spontaneous Assembly Systems. *Adv. Mater.* **2022**, *34*, 2108289.

(49) Zhang, S. Q.; Mu, X. Y.; Li, L.; Yan, L. Q.; Wu, X. Z.; Lei, C. H. Rationally Designed Small Molecular Photoswitches Based on the ESIPT mechanism of Salicylaldehyde Hydrazone Derivatives. *Opt. Mater.* **2021**, *122*, 111780.

(50) Volaric, J.; Szymanski, W.; Simeth, N. A.; Feringa, B. L. Molecular Photoswitches in Aqueous Environments. *Chem. Soc. Rev.* **2021**, *50*, 12377−12449.

(51) Kortekaas, L.; Simke, J.; Arndt, N. B.; Bockmann, M.; Doltsinis, N. L.; Ravoo, B. J. Acid-Catalysed Liquid-to-Solid Transitioning of Arylazoisoxazole Photoswitches. *Chem. Sci.* **2021**, *12*, 11338−11346.

(52) Mengots, A.; Erbs Hillers-Bendtsen, A.; Doria, S.; Ørsted Kjeldal, F.; Machholdt Høyer, N.; Ugleholdt Petersen, A.; Mikkelsen, K. V.; Di Donato, M.; Cacciarini, M.; Brøndsted Nielsen, M. Dihydroazulene-Azobenzene-Dihydroazulene Triad Photoswitches. *Chem.—Eur. J.* **2021**, *27*, 12437−12446.

(53) He, Y. X.; Shangguan, Z. C.; Zhang, Z. Y.; Xie, M. C.; Yu, C. Y.; Li, T. Azobispyrazole Family as Photoswitches Combining (Near-) Quantitative Bidirectional Isomerization and Widely Tunable Thermal Half-Lives from Hours to Years. *Angew. Chem., Int. Ed.* **2021**, *60*, 16539−16546.

(54) Yao, J. B.; Wu, W. H.; Xiao, C.; Su, D.; Zhong, Z. H.; Mori, T.; Yang, C. Overtemperature-Protection Intelligent Molecular Chiroptical Photoswitches. *Nat. Commun.* **2021**, *12*, 2600.

(55) Lvov, A. G.; Bredihhin, A. Azulene as an Ingredient for Visible-Light- and Stimuli-Responsive Photoswitches. *Org. Biomol. Chem.* **2021**, *19*, 4460−4468.

(56) Donaldson, L. Boosting Solar Energy Conservation Using Photoswitches. *Mater. Today* **2021**, *43*, 6−7.

(57) Kolmar, T.; Bullmann, S. M.; Sarter, C.; Hofer, K.; Jaschke, A. Development of High-Performance Pyrimidine Nucleoside and

Oligonucleotide Diarylethene Photoswitches. *Angew. Chem., Int. Ed.* **2021**, *60*, 8164–8173.

(58) Lameijer, L. N.; Budzak, S.; Simeth, N. A.; Hansen, M. J.; Feringa, B. L.; Jacquemin, D.; Szymanski, W. General Principles for the Design of Visible-Light-Responsive Photoswitches: Tetra-ortho-Chloro-Azobenzenes. *Angew. Chem., Int. Ed.* **2020**, *59*, 21663–21670.

(59) Orrego-Hernandez, J.; Dreos, A.; Moth-Poulsen, K. Engineering of Norbornadiene/Quadricyclane Photoswitches for Molecular Solar Thermal Energy Storage Applications. *Acc. Chem. Res.* **2020**, *53*, 1478–1487.

(60) Naren, G.; Hsu, C. W.; Li, S. M.; Morimoto, M.; Tang, S. C.; Hernando, J.; Guirado, G.; Irie, M.; Raymo, F. M.; Sunden, H.; Andreasson, J. An All-Photonic Full Color RGB System Based on Molecular Photoswitches. *Nat. Commun.* **2019**, *10*, 3996.

(61) Tochitsky, I.; Kienzler, M. A.; Isacoff, E.; Kramer, R. H. Restoring Vision to the Blind with Chemical Photoswitches. *Chem. Rev.* **2018**, *118*, 10748–10773.

(62) Qian, Z. Y.; Kang, S. H.; Rajaram, V.; Cassella, C.; McGruer, N. E.; Rinaldi, M. Zero-Power Infrared Digitizers Based on Plasmonically Enhanced Micromechanical Photoswitches. *Nat. Nanotechnol.* **2017**, *12*, 969–973.

(63) Kucharski, T. J.; Ferralis, N.; Kolpak, A. M.; Zheng, J. O.; Nocera, D. G.; Grossman, J. C. Templated Assembly of Photoswitches Significantly Increases the Energy-Storage Capacity of Solar Thermal Fuels. *Nat. Chem.* **2014**, *6*, 441–447.

(64) Szymanski, W.; Beierle, J. M.; Kistemaker, H. A. V.; Velema, W. A.; Feringa, B. L. Reversible Photocontrol of Biological Systems by the Incorporation of Molecular Photoswitches. *Chem. Rev.* **2013**, *113*, 6114–6178.

(65) Lin, Y. K.; Ting, H. W.; Wang, C. Y.; Gwo, S.; Chou, L. J.; Tsai, C. J.; Chen, L. J. Au Nanocrystal Array/Silicon Nanoantennas as Wavelength-Selective Photoswitches. *Nano Lett.* **2013**, *13*, 2723–2731.

(66) Zhu, M. Y.; Zhou, H. C. Azobenzene-Based Small Molecular Photoswitches for Protein Modulation. *Org. Biomol. Chem.* **2018**, *16*, 8434–8445.

(67) Niwano, H.; Nakata, M.; Thisayukta, J.; Link, D. R.; Takezoe, H.; Watanabe, J. Chiral Memory on Transition Between the B2 and B4 phases in an Achiral Banana-Shaped Molecular System. *J. Phys. Chem. B* **2004**, *108*, 14889–14896.

(68) Thompson, M. P.; Hegmann, T.; Wand, M. D.; Lemieux, R. P. Ferroelectric liquid Crystal Dopants with a Chiral (*R,R*)-2,3-difluorooctyloxy Side-Chain: Host Dependence of the Polarization Power. *Liq. Cryst.* **2007**, *34*, 987–994.

(69) Schubert, C. P. J.; Muller, C.; Wand, M. D.; Giesselmann, F.; Lemieux, R. P. Electroclinic Effect in a Chiral Carbosilane-Terminated 5-Phenylpyrimidine Liquid Crystal with 'de Vries-like' Properties. *Chem. Commun.* **2015**, *51*, 12601–12604.

(70) Petrova, S. S.; Chichinadze, N. M.; Shaverdova, V. G. Kinetics of the Weigert Effect in Azo Dyes Embedded in Polymeric Matrices with Different Activities. *Tech. Phys.* **2005**, *50*, 227–231.

(71) Zhang, C.; Fu, G.; Zhu, Y.; Fu, R.; Zhang, G. Microscopical Mechanism of Weigert Effect. *Optik* **1990**, *84*, 119–122.

(72) Dominguez-Candela, I.; Zulkhairi, I.; Pintre, I.; Aripin, N. F. K.; Lora-Garcia, J.; Fombuena, V.; Ros, M. B.; Martinez-Felipe, A. Light-Responsive Bent-Core Liquid Crystals as Candidates for Energy Conversion and Storage. *J. Mater. Chem. C* **2022**, *10*, 18200–18212.

(73) Qi, H.; O'Neil, J.; Hegmann, T. Chirality Transfer In Nematic Liquid Crystals Doped with (*S*)-Naproxen-Functionalized Gold Nanoclusters: An Induced Circular Dichroism Study. *J. Mater. Chem.* **2008**, *18*, 374–380.

(74) Hexemer, A.; Bras, W.; Glossinger, J.; Schaible, E.; Gann, E.; Kirian, R.; MacDowell, A.; Church, M.; Rude, B.; Padmore, H. A SAXS/WAXS/GISAXS Beamline with Multilayer Monochromator. *J. Phys. Conf.* **2010**, *247*, 012007.

(75) Ilavsky, J. Nika: Software for Two-Dimensional Data Reduction. *J. Appl. Crystallogr.* **2012**, *45*, 324–328.

(76) Taugerbeck, A.; Booth, C. J. Design and Synthesis of Chiral Nematic Liquid Crystals. In *Handbook of Liquid Crystals*; Goodby, J.,

Collings, P. J., Kato, T., Tschierske, C., Gleeson, H., Raynes, P., Eds.; Wiley-VCH Weinheim, 2014; pp 1–63.

(77) Walba, D. M.; Eshdat, L.; Korblova, E.; Shoemaker, R. K. On the Nature of the B4 Banana Phase: Crystal or Not a Crystal? *Cryst. Growth Des.* **2005**, *5*, 2091–2099.

(78) Chen, D.; Maclennan, J. E.; Shao, R.; Yoon, D. K.; Wang, H. T.; Korblova, E.; Walba, D. M.; Glaser, M. A.; Clark, N. A. Chirality-Preserving Growth of Helical Filaments in the B4 Phase of Bent-Core Liquid Crystals. *J. Am. Chem. Soc.* **2011**, *133*, 12656–12663.

(79) Otani, T.; Araoka, F.; Ishikawa, K.; Takezoe, H. Enhanced Optical Activity by Achiral Rod-Like Molecules Nanosegregated in the B-4 Structure of Achiral Bent-Core Molecules. *J. Am. Chem. Soc.* **2009**, *131*, 12368–12372.

(80) Araoka, F.; Sugiyama, G.; Ishikawa, K.; Takezoe, H. Electric-field controllable optical activity in the nano-segregated system composed of rod- and bent-core liquid crystals [Invited]. *Opt. Mater. Express* **2011**, *1*, 27–35.

(81) Callahan, R. A.; Coffey, D. C.; Chen, D.; Clark, N. A.; Rumbles, G.; Walba, D. M. Charge Generation Measured for Fullerene-Helical Nanofilament Liquid Crystal Heterojunctions. *ACS Appl. Mater. Interfaces* **2014**, *6*, 4823–4830.

(82) Lee, J. J.; Kim, B. C.; Choi, H. J.; Bae, S.; Araoka, F.; Choi, S. W. Inverse Helical Nanofilament Networks Serving as a Chiral Nanotemplate. *ACS Nano* **2020**, *14*, 5243–5250.

(83) Cao, Y.; Tan, T. Y.; Walba, D. M.; Clark, N. A.; Ungar, G.; Zhu, C. H.; Zhang, L.; Liu, F. Understanding and Manipulating Helical Nanofilaments in Binary Systems with Achiral Dopants. *Nano Lett.* **2022**, *22*, 4569–4575.

(84) Chen, D.; Tuchband, M. R.; Horanyi, B.; Korblova, E.; Walba, D. M.; Glaser, M. A.; Maclennan, J. E.; Clark, N. A. Diastereomeric liquid crystal domains at the mesoscale. *Nat. Commun.* **2015**, *6*, 7763.

(85) Liu, J.; Molard, Y.; Prévôt, M. E.; Hegmann, T. Highly Tunable Circularly Polarized Emission of an Aggregation-Induced Emission Dye Using Helical Nano- and Microfilaments as Supramolecular Chiral Templates. *ACS Appl. Mater. Interfaces* **2022**, *14*, 29398–29411.

(86) Kim, B. C.; Choi, H. J.; Lee, J. J.; Araoka, F.; Choi, S. W. Circularly Polarized Luminescence Induced by Chiral Super Nanospaces. *Adv. Funct. Mater.* **2019**, *29*, 1903246.

(87) Liu, J.; Shadpour, S.; Nemati, A.; Prévôt, M. E.; Hegmann, E.; Zhu, C. H.; Hegmann, T. Binary Mixtures of Bent-Core Molecules Forming Distinct Types of B4 Phase Nano- and Microfilament Morphologies. *Liq. Cryst.* **2021**, *48*, 1129–1139.

(88) Hough, L. E.; Spannuth, M.; Nakata, M.; Coleman, D. A.; Jones, C. D.; Dantlgraber, G.; Tschierske, C.; Watanabe, J.; Korblova, E.; Walba, D. M.; Maclennan, J. E.; Glaser, M. A.; Clark, N. A. Chiral Isotropic Liquids from Achiral Molecules. *Science* **2009**, *325*, 452–456.